Korean J. Chem. Eng., 37(8), 1371-1378 (2020)
DOI: 10.1007/s11814-020-0610-6

pISSN: 0256-1115
eISSN: 1975-7220

Porous an hollow nanofibers for solid oxide fuel cell electrodes

Minwoo Ahn, Sangyeon Hwang, Seungwoo Han, Mingi Choi, Doyoung Byun†, and Wonyoung Lee†

Department of Mechanical Engineering, Sungkyunkwan University, Suwon 16419, Korea
(*Received 21 March 2020 • Revised 21 May 2020 • Accepted 8 June 2020*)

Abstract−Among the diverse approaches for improving the electrode performance of solid oxide fuel cells operating at intermediate temperatures, the use of nanofiber-based electrodes has provided large improvement owing to their large specific surface area, continuous conduction pathway, and highly porous structure. However, the low thermal stability at increased temperature often limits the process compatibility and sustainability during operation. In this study, we fabricated nanofiber-based electrodes with a high porosity and hollow shape using one-step electrospinning with a hydrogel polymer, which exhibited largely improved performance and excellent thermal stability. A porous-nanofiber-based cell exhibits a polarization resistance of 0.021 Ωcm^2 and maximum power density of 1.71 W/cm^2 at 650 °C, which is an improvement of 34.3% and 14.7% compared to that of a solid-nanofiber-based cell, respectively. Comprehensive analyses of the microstructures and chemistry indicate that the performance increase is mainly attributable to the enhanced surface oxygen exchange reactions owing to the extended reaction sites with lower energy barriers by the high porosity and enriched oxygen vacancies in the nanofibers.

Keywords: Solid Oxide Fuel Cell, Electrode, Nanofiber, Porous Structure, Grain Boundary

INTRODUCTION

Nanofibers have been extensively investigated for various applications, including fuel cells [1-4], secondary batteries [5,6], and gas sensors [7,8] owing to various structural advantages including the large specific surface areas, continuous conduction pathways, and highly porous structures, originating from the one-dimensional characteristics and randomly distributed network. In particular, for solid oxide fuel cells (SOFCs) operating at intermediate temperatures (ITs, 500-700 °C), nanofiber-based electrodes have provided substantial improvements in oxygen reduction reaction (ORR) kinetics at the cathodes, which is one of the most challenging issues in the development of IT-SOFCs, primarily because of their high porosity and large specific surface area [2,3,9-12].

Numerous fabrication methods have been developed for the syntheses of porous nanofibers with higher porosity and larger specific surface area for further improvement [2,4,13,14]. For example, porous nanofibers can be die-cast using polymer templates with specific geometries, which yields high productivity and repeatability by the control of the casting solution for the structur and materials of the nanofibers [13,14]. However, the diameters of the fabricated nanofibers are relatively large (500-800 nm) because they are limited by the pore sizes of the polymer templates, which hinders the increase in number of reaction sites owing to the small specific surface area and packing density. The most typical method for the fabrication of porous nanofibers involves a decreased sintering temperature (e.g., below 800 °C for cobalt-based oxides) [4,11,13]. The nitrate precursors in as-spun nanofibers transform into oxides during the sintering in ambient air and spontaneously form porous nanofibers owing to the different diffusivities of the nitrate precursors and oxides [15]. The fabricated nanofibers exhibit not only large specific surface areas for an increased number of reaction sites owing to the high porosity, but also nanocrystalline structure, including a high density of grain boundaries with enriched oxygen vacancies, which provide a substantially improved polarization resistance when they are utilized as SOFC electrodes [4,11,13]. However, the low sintering temperature hinders the compatibility with the conventional postprocesses that typically require sintering temperatures higher than 900 °C for sufficient interfacial adhesion and connectivity among electrode materials because the high porosity and nanocrystalline structure would be destroyed with the grain growth [2,9,10,16-23]. Therefore, a fabrication process retaining the high porosity of the nanofibers at a reasonably high sintering temperature is required to fully utilize the superior characteristics of the porous nanofibers.

In this study, we synthesized porous nanofibers by one-step electrospinning at higher fabrication temperature up to 1,000 °C for electrodes of IT-SOFCs. Gelatin was introduced and compared to the conventionally used polyvinylpyrrolidone (PVP) for the fabrication of the electrospun nanofibers. $Sm_{0.5}Sr_{0.5}CoO_{3-\delta}$ (SSC) was used as an electrode material owing to its relatively high ionic and electronic conductivities, fast surface oxygen exchange, low overpotential at an IT [24-26], and chemical compatibility with $Gd_{0.2}Ce_{0.8}O_{1.9}$ (GDC), a common electrolyte material for IT-SOFCs. The nanofibers fabricated at sintering temperatures up to 1,000 °C with gelatin exhibited porous and hollow morphology, while those fabricated at sintering temperatures higher than 900 °C with PVP exhibited solid morphology. A porous-nanofiber-based single cell exhibited a polarization resistance (R_p) of 0.021 Ωcm^2 and maximum power density of 1.71 W/cm^2 at 650 °C, which are improvements of 34.3% and 14.7%, respectively, compared to those of a solid-nanofiber-based single cell. The improved electrochemical performance was well maintained without considerable reduction for 200 h at 650 °C. Struc-

†To whom correspondence should be addressed.
E-mail: dybyun@skku.edu, leewy@skku.edu

tural and chemical analyses reveal that the surface oxygen exchange reaction originated mainly from the extended reaction sites with lower energy barriers owing to the high porosity and enriched oxygen vacancies in the nanofibers. Our results are valuable for the fabrication of nanofiber-based electrodes for IT-SOFCs with high performance and stability.

EXPERIMENTAL METHODS

1. Synthesis of PVP and Gelatin Nanofibers

The nanofibers were fabricated using one-step electrospinning and subsequent sintering at 900 °C for 3 h for phase formation. Deionized water, ethanol, and acetic acid were mixed in a volumetric ratio of 1 : 1 : 3. 10 wr% PVP (Sigma Aldrich) and 22 wt% gelatin (Sigma Aldrich) were added to the PVP- and gelatin-based nanofibers (pNFs and gNFs, respectively) for appropriate solution viscosity. $Sm(NO_3)_3 \cdot 6H_2O$, $Sr(NO_3)_2$, and $Co(NO_3)_2 \cdot 6H_2O$ (Sigma Aldrich) were dissolved in the solution in a molar ratio of 0.5 : 0.5 : 1 to form the SSC perovskite phase as an electrode material. The solution was stirred at 60 °C overnight on a hot plate for complete dissolution. The precursor solution was loaded into a syringe pump with a gauge needle (NanoNC; NNC-PN-34GA). Electrospinning was carried out at an electric field of 0.75 kV/cm and flow rate of 1.2 mL/h. A grounded aluminum foil was used to collect the electrospun nanofibers [4,27].

2. Symmetric Cell Fabrication

GDC powders (Rhodia, 15Y022301) were pressed at 40 MPa and sintered at 1,500 °C for 5 h to form dense disk-like GDC pellets with diameter of 1 cm and thickness of ~1.1 mm. SSC powders (Kceracell; K150703-SSC-163) were ball-milled with ethanol overnight for a uniform size distribution. After drying at 80 °C for 3 h, SSC powders mixed with a binder (VEH, Fuel Cell Materials) were screen-printed symmetrically on both sides of the GDC pellets to a thickness of ~5 μm to provide common interfacial adhesion [4]. The specific role and optimization process of SSC powder layer between electrolyte and fiber electrode was investigated in previous reports [4]. Calcined pNFs and gNFs were mixed with the same binder and screen-printed on top of the SSC powder layers to thickness of ~8 μm. For an effective current collection, SSC powders were screen-printed on the nanofiber layer with a thickness of ~3 μm. The fabricated symmetric cells were sintered at 900 °C for 3 h.

3. Single Cell Fabrication

For the performance test, a single cell was fabricated with an anode-supported configuration. NiO (Kojundo Chemical), GDC (Grand Chemical & Material), and carbon black (Alfa Aesar, 1333-86-4) were homogenously mixed using ball milling for 24 h in a weight ratio of 6 : 4 : 0.3, with a dispersant (HypermerTM KD-6, Croda), plasticizer (dibutyl phthalate), and polyvinyl butyral binder. The fabricated anode powder was uniaxially pressed to a thickness of ~1 mm and presintered at 900 °C to obtain mechanical strength. For the anode functional layer (AFL), NiO and GDC powder in a weight ratio of 6 : 4 were mixed with the binder and spin-coated to a thickness of ~8 μm. The slurry was prepared by mixing GDC powder with ethanol solvent, dispersant (DISPERBYK-2012), and ethyl cellulose binder. The electrolyte layer was fabricated by spin coating to a thickness of ~5 μm. The AFL and electrolyte were cosintered at 1,400 °C. The cathode layer was fabricated in the same manner as that for the symmetric cell fabrication.

4. Characterization of Materials

Field-emission scanning electron microscopy (FE-SEM, JSM7000F, JEOL) was used to analyze the morphology of the nanofibers. The specific surface area was measured using the Brunauer-Emmett-Teller (BET) isothermal technique with nitrogen adsorption using a surface area analyzer (BELSORP mini-II, BEL Japan, Inc.). The crystal structure of the nanofibers was characterized by X-ray diffraction (XRD, Expert Pro-MPD, PANalytical) using the PANalytical X'Pert HighScore Plus software with Cu K_α radiation (0.15418 nm). The chemical composition of the nanofibers was measured using X-ray photoelectron spectroscopy (XPS) (K-Alpha, Al K_α μ-

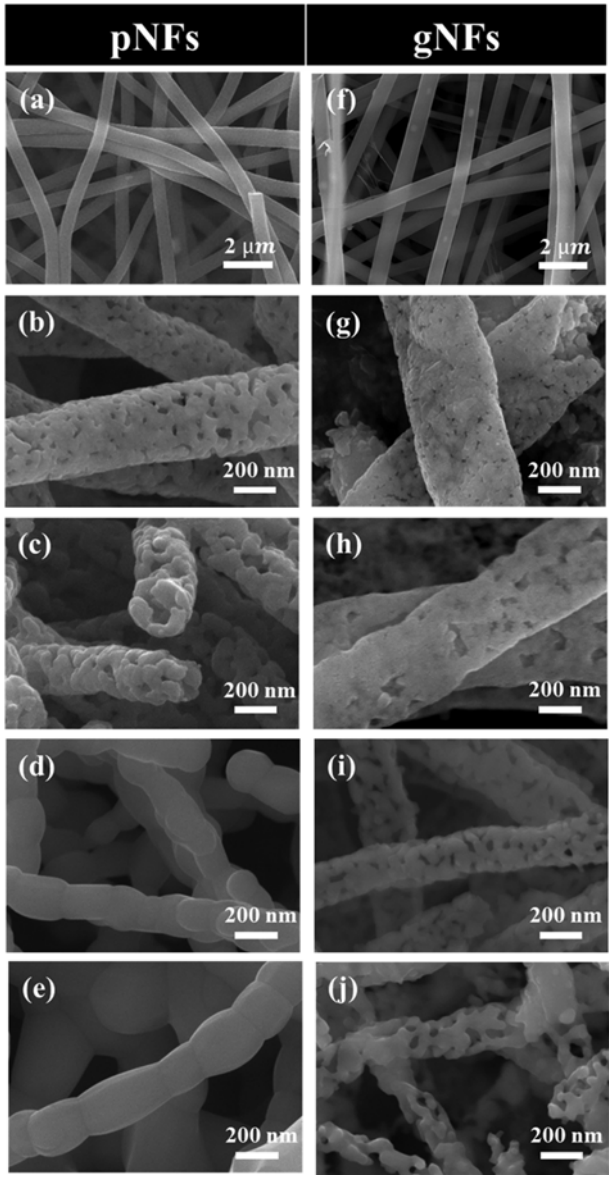

Fig. 1. SEM images of ((a), (f)) as-spun nanofibers and nanofibers calcined at sintering temperatures of ((b), (g)) 700, ((c), (h)) 800, ((d), (i)) 900, and ((e), (j)) 1,000 °C with PVP and gelatin, respectively.

focused monochromator, 1,486.6 eV). Electrochemical impedance spectroscopy (EIS) measurements were performed using a custom-made test station in ambient air with an impedance analyzer (GAMRY Reference 600, GAMRY) in the frequency range of 10^{-2} to 10^{6} Hz at an alternating current amplitude of 30 mV in the temperature range of 650 to 500 °C with an interval of 50 °C.

RESULTS AND DISCUSSION

The structure of the electrospun nanofibers, such as the shape and porosity, strongly depended on the sintering temperature [4,13,28]. To evaluate the effects of the sintering temperature on the structure of the nanofibers, one-step electrospinning was conducted with two different polymers, PVP and gelatin. The sintering temperature was in the range of 700-1,000 °C. The as-spun nanofibers exhibited solid and smooth shapes with diameters of 600-700 nm; no considerable structural differences were observed between pNFs and gNFs, as shown in Fig. 1(a) and 1(f), respectively [27]. However, the structure of the calcined nanofibers considerably depended on the sintering temperature and polymer. The sintering temperature range of 700 to 1,000 °C was used because the lowest temperature of 700 °C is required to form the perovskite SSC phase [4,11]. Fig. 1(b)-(e) shows the structural evolution of the calcined pNFs, from the porous hollow shape to the smooth solid shape, with the increase in sintering temperature from 700 to 1,000 °C. With the shape change, the diameter of the calcined pNF decreased from 650 to 220 nm, while the BET specific surface area decreased from 20.73 to 10.68 m^2/g. gNFs exhibited porous hollow shapes at the sintering temperatures of 700-1,000 °C, as shown in Fig. 1(g)-(j). They maintained similar diameters and specific surface areas of 200-250 nm and 15.5-17.1 m^2/g, respectively. The structure of pNFs and gNFs exhibited considerable differences at sintering temperatures higher than 900 °C. For example, at the sintering temperature of 900 °C, gNFs exhibited porous hollow shape with a specific surface area of 16.61 m^2/g, while pNFs exhibited smooth solid shape with a specific surface area of 12.19 m^2/g. In general, with the increase in sintering temperature, the surface area decreased owing to the grain growth and agglomeration with the thermal energy [4]. Unlike PVP consisting of simple ionomers, gelatin has three-dimensional bonding structure with a higher decomposition temperature [29,30], and thus gNFs maintained a porous structure at the high sintering temperature with suppressed grain growth and agglomeration.

To further investigate the effects of the sintering temperature on the electrospun nanofibers with different polymers, an XRD analysis was carried out as a function of the sintering temperature and polymer. Fig. 2(a) shows XRD patterns of pNFs and gNFs after the sintering at 700, 800, 900, and 1,000 °C. pNFs exhibited orthorhombic perovskite phases at all sintering temperatures without impurity phase [4]. gNFs also exhibited the orthorhombic perovskite phase at sintering temperature higher than 900 °C. However, small amounts of binary oxide phases such as Sm_2O_3, SrO, and Co_3O_4 were observed at the sintering temperature of 700 and 800 °C. These binary oxides may be intermediate products between the initial metal precursors and perovskite oxides [31]. Fig. 2(b) presents the quantitative weight fractions of the perovskite and nonperovskite

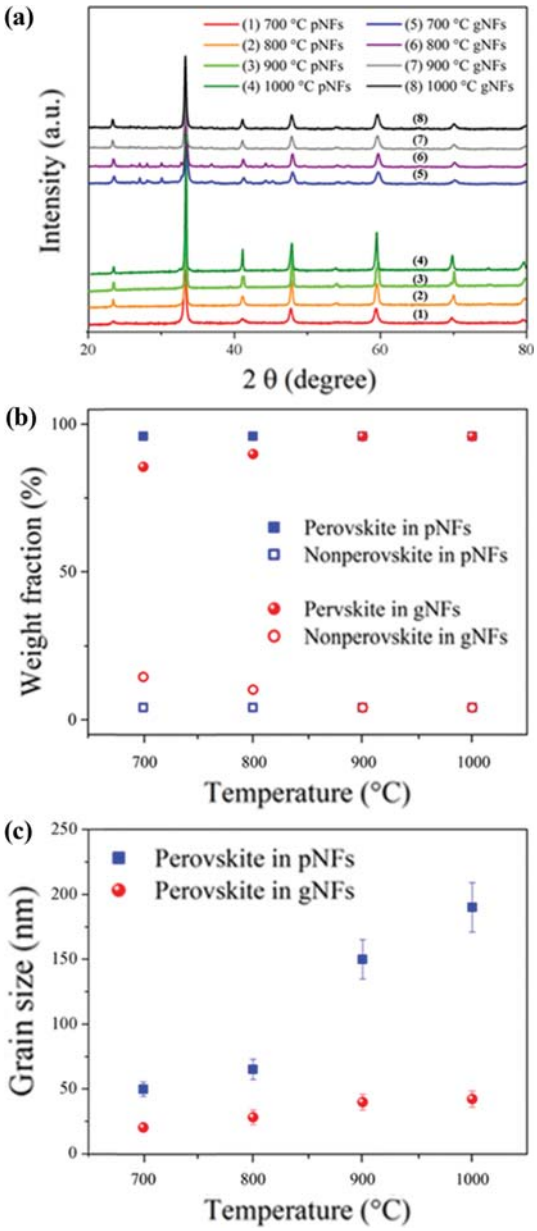

Fig. 2. (a) XRD patterns of the nanofibers calcined at the sintering temperatures of 700 to 1,000 °C, at intervals of 100 °C, (b) weight fractions of the perovskite and non-perovskite phases in pNFs and gNFs, and (c) calculated grain sizes of the perovskite phases in pNFs and gNFs.

phases in pNFs and gNFs, calculated by Rietveld fitting [11,32]. pNFs exhibited the pure perovskite phase at the sintering temperature of 700 to 1,000 °C, while gNFs exhibited the pure perovskite phase above 900 °C and binary oxide phase content of 11.3 and 6.6 wt% at the sintering temperature of 700 and 800 °C, respectively. The higher sintering temperature required for full crystallization of the SSC phases in gNFs can explain the higher porosity of gNFs at the same sintering temperature than that of pNFs, as shown in Fig. 1. The higher sintering temperature of gNFs (900 °C) than that of pNFs (700 °C) required for full crystallization is not a serious issue because a sintering temperature of 900 °C (or higher) is nec-

essary in post-processes to fabricate actual full cells for sufficient interfacial adhesion and connectivity of the ceramic materials [2,9, 10,16-23]. Fig. 2(c) shows the calculated grain sizes of the perovskite phases in pNFs and gNFs as functions of the sintering temperature. The grain size increased with the sintering temperature in both nanofibers. However, the grain sizes of gNFs were substantially smaller than those of pNFs at all sintering temperatures. In particular, the grain size of pNFs abruptly increased from 65.3 to 150 nm when the sintering temperature was changed from 800 to 900 °C, while the grain size of gNFs exhibited a moderate increase. The abrupt grain growth at 900 °C is in agreement with the structural change, from the porous hollow shape to the smooth solid shape, as shown in Fig. 1. Therefore, the suppressed grain growth in gNFs can explain the delayed crystallization of the perovskite phase with the porous hollow shapes of the electrospun nanofibers after the sintering at the increased temperature.

The observed changes in microstructures can induce changes in distributions of charged defects in the nanofibers. In particular, the smaller grain size in gNFs can lead to a higher concentration of oxygen vacancies because the lattice oxygen at the grain boundaries has smaller coordination numbers and the oxygen-to-metal bond can be easily loosened [33,34]. Accordingly, the grain boundaries with the enriched oxygen vacancies could provide more active reaction sites with lower activation energy barriers than the grain core

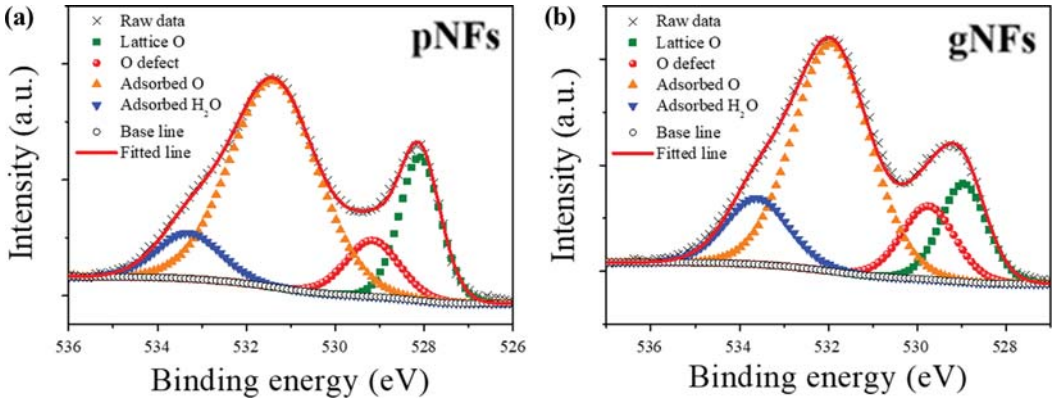

Fig. 3. XPS spectra of O1s peaks for (a) pNFs and (b) gNFs with the sintering temperature of 900 °C.

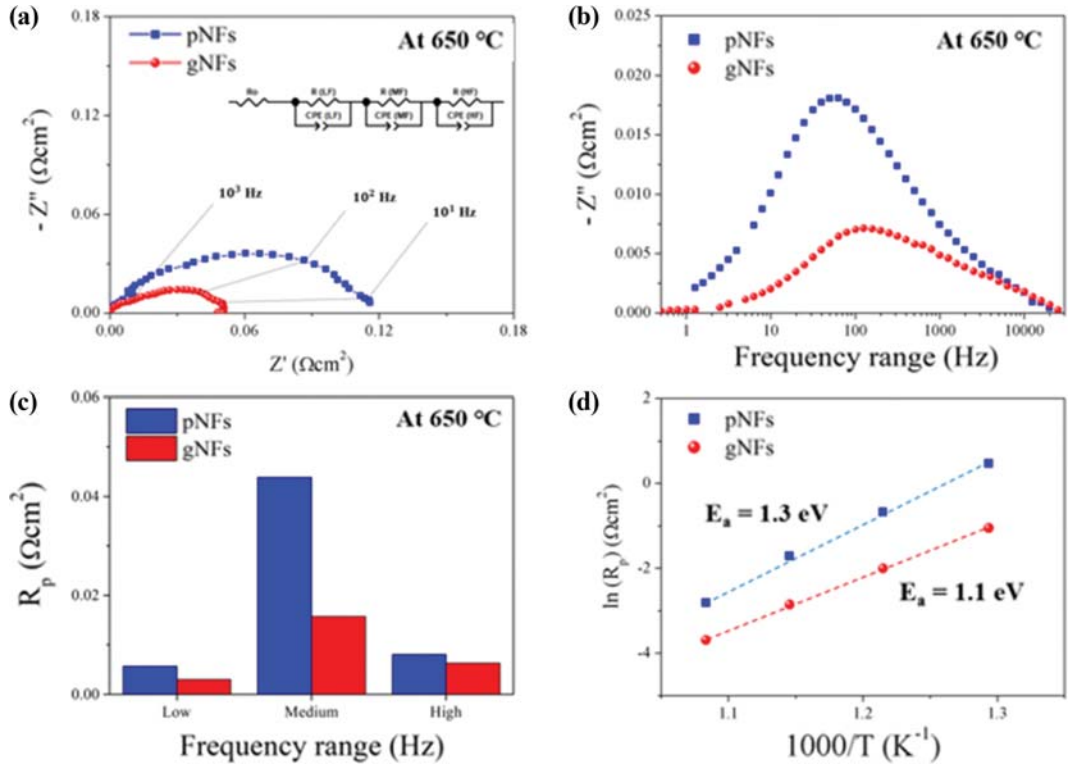

Fig. 4. EIS results for the nanofiber-based electrodes in symmetric cell configurations. (a) Nyquist plots, (b) Bode plots, (c) polarization resistances with relative fractions at each frequency range, and (d) Arrhenius plots.

and thus facilitate the ORR kinetics [33,35-37]. To verify the presence of enriched oxygen vacancies in gNFs with the smaller grain sizes, the XP spectra of the O 1*s* core levels of pNFs and gNFs were deconvoluted into four characteristic peaks of lattice oxygen species (~528.1 eV, $O_{lattice}$), oxygen vacancies (~529.2 eV, V_o), surface-adsorbed oxygen (~531.4 eV, O_2), and adsorbed water molecule (~533.3 eV, H_2O), as shown in Fig. 3(a)-(b) [38-46]. Therefore, the peak intensity of oxygen vacancies normalized by that of lattice oxygen can represent the relative concentration of oxygen vacancies in the nanofibers. The calculated concentrations of oxygen vacancies are 0.51 and 0.85 for pNFs and gNFs, respectively, which show the substantially higher concentration of oxygen vacancies in gNFs, consistent with the smaller grain sizes of gNFs, as shown in Fig. 2(c). Moreover, as shown in Fig. S2, higher ratio of Co^{2+}/Co^{3+} value of ~1.52 in gNFs than that in pNFs (~1.29) further supports the higher intensity of oxygen vacancies in gNFs [45].

To evaluate the effects of the structural and chemical differences on the electrochemical performance, EIS measurements were carried out using the nanofiber-based electrodes fabricated at the sintering temperature of 900 °C in a temperature range of 650-500 °C. The symmetric cell configuration was employed to focus on the cathode and exclude contributions of other components [4]. Fig. 4(a) shows Nyquist plots of the pNF- and gNF-based electrodes measured at 650 °C. The polarization resistance (R_p) of the pNF-based electrode was 0.06 Ωcm^2, consistent with the reported value [11], while the gNF-based electrode exhibited R_p reduced by 58% (0.025 Ωcm^2). Fig. 4(b) shows Bode plots measured at 650 °C to identify each electrode reaction by the specific peak frequency [24,47,48]. Generally, a specific ORR process can be clarified with the frequency range of high-frequency (HF, >10^3 Hz), medium-frequency (MF, 10^1-10^3 Hz), and low-frequency (LF, <10^1 Hz), representing the charge transport, surface oxygen exchange, and gas diffusion, respectively [49-51]. Therefore, the imaginary components of the gNF-based electrode were largely suppressed in the MF range, which indicates a significant improvement in surface oxygen exchange reaction at the cathode.

The imaginary components of the gNF-based electrode were largely suppressed in the medium-frequency (MF, 10^1-10^3 Hz) range, which indicates a significant improvement in surface oxygen exchange reaction at the cathode [4,21]. The shift of the peak frequency to the higher frequency in the Bode plot from 60.1 Hz for the pNF-based electrode to 125.5 Hz for the gNF-based electrode supports the claim of facilitated surface oxygen exchange reactions in gNF-based electrodes [10,52]. Fig. 4(c) shows the R_p values of the nanofiber-based electrodes at each frequency range. The Nyquist plots were fitted using the Z-view fitting program into three parallel resistance–constant-phase-element equivalent circuits; the results are listed in Table S1. The MF response predominantly contributed to the total R_p for both electrodes. However, the gNF-based electrode exhibited a substantial reduction in MF response compared to the high-frequency and low-frequency responses, which confirms that the increase in R_p originated from mainly the facilitated surface oxygen exchange reactions. Fig. 4(d) shows Arrhenius plots of the nanofiber-based electrodes measured at 650-500 °C. The derived activation energy (E_a) of the pNF-based electrode (1.3±0.06 eV) indicates that the surface oxygen exchange reactions were the rate-determining step [11,21]. The reduced E_a of the gNF-based electrode (1.1±0.05 eV) indicates a smaller relative contribution of the surface oxygen exchange reactions to the total R_p, which led to larger relative contributions of the oxygen ion bulk conduction and oxygen ion transport at the interfaces with E_a of 0.94±0.03 eV [48,53,54]. Therefore, the improvement in R_p of the gNF-based electrode can be attributed to mainly the surface oxygen exchange reactions enhanced by the high porosity and small grain size of gNFs. The high porosity of gNFs can provide an increased number of reaction sites with the large specific surface area. The small grain size or enriched oxygen vacancies of gNFs can provide active reaction sites with lower activation energies.

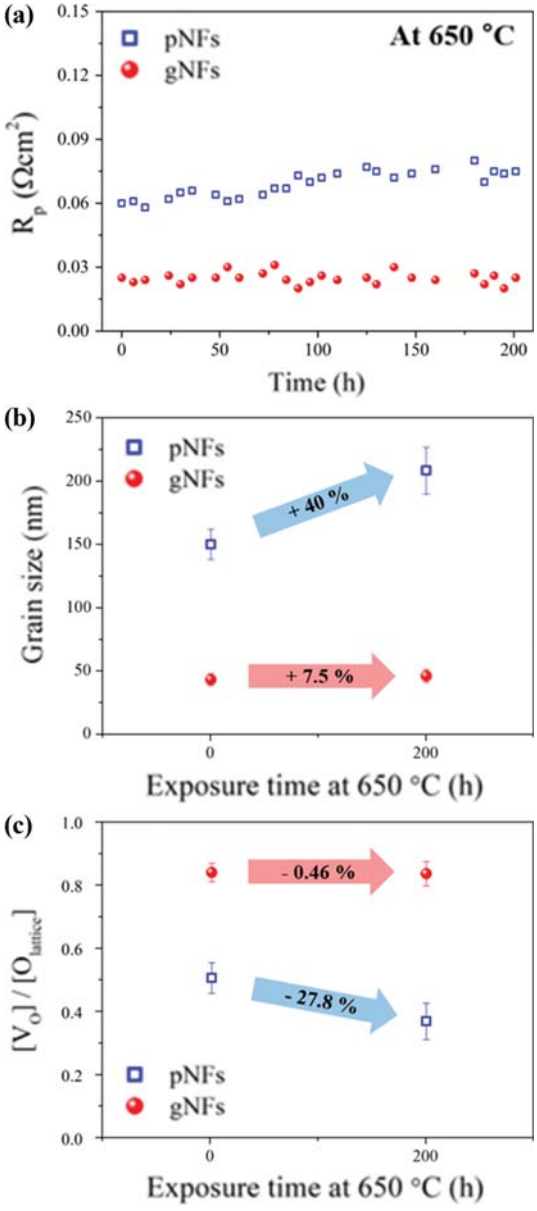

Fig. 5. Stability test for 200 h at 650 °C. (a) Changes in R_p values of the nanofiber-based electrodes, (b) changes in grain sizes, and (c) normalized oxygen vacancy concentrations before and after the test.

The thermal stability of the electrochemical, structural, and chemical properties of the nanofiber-based electrodes was evaluated. Fig. 5(a) shows the R_p values at 650 °C for 200 h in the symmetric cell configuration to focus on the nanofiber-based electrodes and exclude degradations by other components. The pNF-based electrode exhibited an increase in R_p from 0.06 to 0.075 Ωcm^2 with a degradation rate of 0.125%/h, while the gNF-based electrode did not exhibit considerable degradation for 200 h. Fig. 5(b) shows the grain sizes calculated using the XRD analysis before and after the stability test. The grain size of pNFs exhibited a considerable increase from 150 to 210 nm, while that of gNFs was almost unchanged (40 to 43 nm). Fig. 5(c) shows the normalized concentrations of oxygen vacancies evaluated by the XPS analysis before and after the stability test. The normalized concentration of oxygen vacancies in pNFs decreased by 27.8%, while that in gNFs was unchanged. In addition, the specific surface area of pNFs calculated using the BET measurement results decreased from 12.19 to 10.98 m^2/g, while that of gNFs was unchanged. The observed changes and differences between pNFs and gNFs can be attributed to the grain growth during the operation at 650 °C for 200 h. Even though the operation temperature (650 °C) was lower than the sintering temperature (900 °C), the grains in pNFs became larger, which led to the decrease in specific surface area, decrease in concentration of oxygen vacancies, and hence increase in R_p. In contrast, the grain growth in gNFs was largely suppressed, which led to a stable R_p at 650 °C for 200 h. These results demonstrate the excellent thermal stability of gNFs and largely enhanced ORR kinetics.

Fig. 6 compares the electrochemical performance of the nanofiber-based electrodes at 650 °C in anode-supported single cell configurations. A cross-sectional SEM image of the single cell is presented in Fig. S1. Fig. 6(a) shows the increase in maximum power density of 14.7%, from 1.49 W/cm^2 for the pNF cell to 1.71 W/cm^2 for the gNF cell. Fig. 6(b) shows Nyquist plots measured at 650 °C at the open-circuit voltage. The ohmic resistances were not considerably different, 0.055 and 0.059 Ωcm^2 for the pNF and gNF cells, respectively. However, R_p decreased by 34.3%, from 0.032 Ωcm^2 for the pNF cell to 0.021 Ωcm^2 for the gNF cell. Fig. 6(c) and 6(d) show Arrhenius plots for the pNF and gNF cells measured at 650-500 °C in the anode-supported single cell configurations. The derived activation energies for the ohmic resistance ($E_{a,o}$), polarization resistance ($E_{a,p}$), and total resistance ($E_{a,t}$) are listed in Table 1. The $E_{a,o}$ values were similar, 0.39 eV for the pNF cell and 0.38 eV for the gNF cell, which indicates the absence of effects of the nanofiber differences on the ohmic resistance. However, $E_{a,p}$ was considerably decreased, from 1.25 eV for the pNF cell to 1.08 eV for the gNF cell, which led to the decrease in $E_{a,t}$, from 0.91 eV for the pNF cell to 0.72 eV for the gNF cell. The decreases in R_p and $E_{a,p}$ and similar R_o and $E_{a,o}$ show that the performance increase originated

Table 1. Activation energy of each resistance of the nanofiber-based single cells

Activation energy (eV)	pNF cell	gNF cell
Ohmic resistance	0.39	0.38
Polarization resistance	1.25	1.08
Total resistance	0.91	0.72

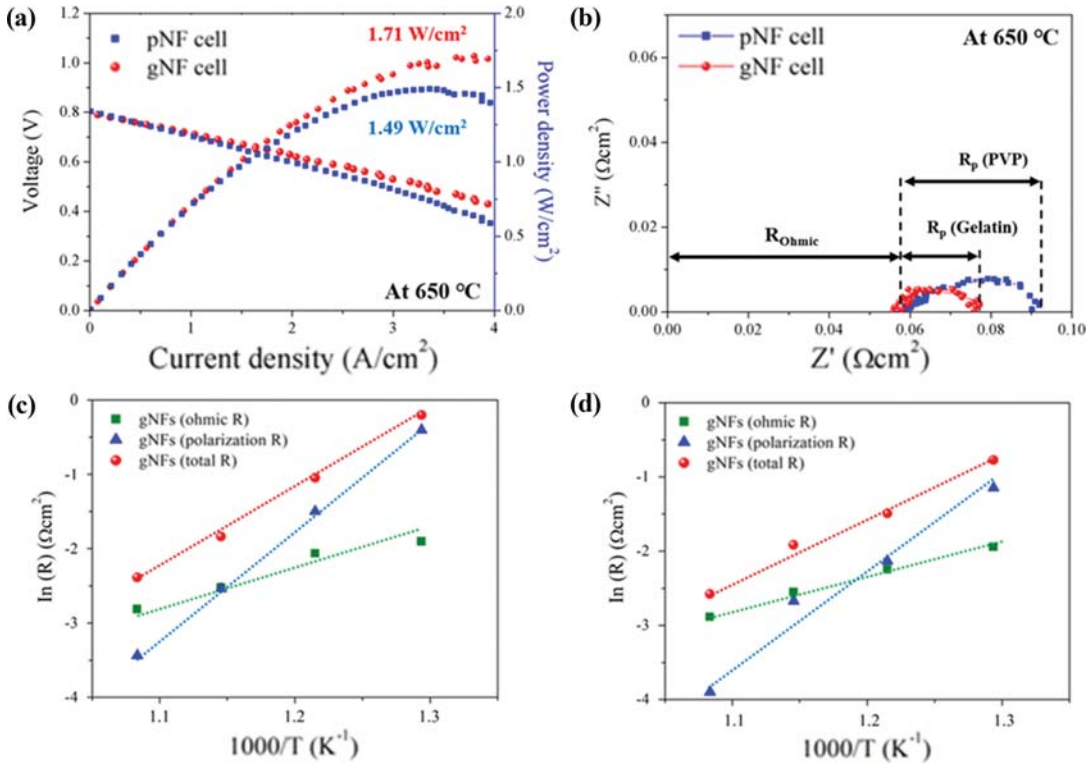

Fig. 6. Electrochemical analysis of the nanofiber-based electrodes in single cell configurations. (a) Current density-voltage curves, (b) Nyquist plots, and Arrhenius plots of the (c) pNF and (d) gNF cells.

from the facilitated ORR kinetics, consistent with the symmetric cell analysis (Fig. 4).

CONCLUSIONS

We demonstrated enhanced ORR kinetics in porous-hollow-nanofiber-based electrodes fabricated by one-step electrospinning for IT-SOFCs. Porous and hollow shapes of the electrospun nanofibers were obtained at high sintering temperatures of up to 1,000 °C. The polarization resistance for surface oxygen reduction reactions was substantially improved with the enlarged surface area and increased number of grain boundaries with enriched oxygen vacancies. In particular, the porous-nanofiber-based cell exhibited a polarization resistance (0.021 Ωcm^2) decreased by 34.3% and maximum power density (1.71 W/cm^2) increased by 14.7% at 650 °C compared to those of the solid-nanofiber-based cell, without considerable degradation for 200 h at 650 °C. These results pave the way for the development of simple strategies for the fabrication of porous-nanofiber-based electrodes for high-performance IT-SOFCs.

ACKNOWLEDGEMENTS

This research was supported by the Basic Science Research Program through the National Research Foundation (NRF) grant funded by the Korea government (MSIP), and Future Planning (Grant No. 2019R1A2C4070158, 2017R1E1A1A01075353), by the Global Frontier R&D program on Center for Multiscale Energy System funded by the NRF under the Ministry of Science, ICT, and Future Planning, Korea (Grant No. NRF-2014M3A6A7074784), and by the Korea Institute of Energy Technology Evaluation and Planning (KETEP) and the Ministry of Trade, Industry & Energy (MOTIE) of the Republic of Korea (No. 20173010032170), and by the Technology Development Program to Solve Climate Changes (2017M1A2A2044927).

NOMENCLATURE

Symbol

E_a : activation energy [eV]
$E_{a,o}$: activation energy for the ohmic resistance [eV]
$E_{a,p}$: activation energy for the polarization resistance [eV]
$E_{a,t}$: activation energy for the total resistance [eV]
R_o : ohmic resistance [Ωcm^2]
R_p : polarization resistance [Ωcm^2]

SUPPORTING INFORMATION

Additional information as noted in the text. This information is available via the Internet at http://www.springer.com/chemistry/journal/11814.

REFERENCES

1. Y. Jeon, J.-h. Myung, S.-h. Hyun, Y.-g. Shul and J. T. S. Irvine, *J. Mater. Chem. A*, **5**, 3966 (2017).
2. Y. Chen, Y. Bu, B. Zhao, Y. Zhang, D. Ding, R. Hu, T. Wei, B. Rainwater, Y. Ding, F. Chen, C. Yang, J. Liu and M. Liu, *Nano Energy*, **26**, 90 (2016).
3. C. Kim, H. Park, I. Jang, S. Kim, K. Kim, H. Yoon and U. Paik, *J. Power Sources*, **378**, 404 (2018).
4. M. Ahn, J. Lee and W. Lee, *J. Power Sources*, **353**, 176 (2017).
5. J.-W. Jung, C.-L. Lee, S. Yu and I.-D. Kim, *J. Mater. Chem. A*, **4**, 703 (2016).
6. L. Qie, W. M. Chen, Z. H. Wang, Q. G. Shao, X. Li, L. X. Yuan, X. L. Hu, W. X. Zhang and Y. H. Huang, *Adv. Mater.*, **24**, 2047 (2012).
7. A. Khalil, J. J. Kim, H. L. Tuller, G. C. Rutledge and R. Hashaikeh, *Sensor. Actuat. B-Chem.*, **227**, 54 (2016).
8. D.-J. Yang, I. Kamienchick, D. Y. Youn, A. Rothschild and I.-D. Kim, *Adv. Funct. Mater.*, **20**, 4258 (2010).
9. J. G. Lee, J. H. Park and Y. G. Shul, *Nat. Commun.*, **5**, 4045 (2014).
10. M. Ahn, S. Han, J. Lee and W. Lee, *Ceram. Int.*, **46**, 6006 (2020).
11. M. Ahn, J. Cho and W. Lee, *J. Power Sources*, **434**, 226749 (2019).
12. J. Y. Koo, Y. Lim, Y. B. Kim, D. Byun and W. Lee, *Int. J. Hydrogen Energy*, **42**, 15903 (2017).
13. M. G. Bellino, J. G. Sacanell, D. G. Lamas, A. G. Leyva and N. E. W. de Reca, *J. Am. Chem. Soc.*, **129**, 3066 (2007).
14. J. Li, N. Zhang, Z. He, K. Sun and Z. Wu, *J. Alloys Compd.*, **663**, 664 (2016).
15. P. Liu, Y. Zhu, J. Ma, S. Yang, J. Gong and J. Xu, *Colloids Surf. A*, **436**, 489 (2013).
16. E. Zhao, X. Liu, L. Liu, H. Huo and Y. Xiong, *Pro. Nat. Sci-Mater.*, **24**, 24 (2014).
17. E. P. Murray, M. J. Sever and S. A. Barnett, *Solid State Ionics*, **148**, 27 (2002).
18. S. Huang, C. Peng and Z. Zong, *J. Power Sources*, **176**, 102 (2008).
19. M. Zhi, S. Lee, N. Miller, N. H. Menzler and N. Wu, *Energy Environ. Sci.*, **5**, 7066 (2012).
20. F. Zhao, R. Peng and C. Xia, *Mater. Res. Bull.*, **43**, 370 (2008).
21. J. Lee, S. Hwang, M. Ahn, M. Choi, S. Han, D. Byun and W. Lee, *J. Mater. Chem. A*, **7**, 21120 (2019).
22. C.-L. Chang, C.-S. Hsu, J.-B. Huang, P.-H. Hsu and B.-H. Hwang, *J. Alloys Compd.*, **620**, 233 (2015).
23. E. Zhao, Z. Jia, X. Liu, K. Gao, H. Huo and Y. Xiong, *Ceram. Int.*, **40**, 14891 (2014).
24. M. Koyama, C.-j. Wen, T. Masuyama, J. Otomo, H. Fukunaga, K. Yamada, K. Eguchi and H. Takahashi, *J. Electrochem. Soc.*, **148**, A795 (2001).
25. M. K. H. Fukunaga, N. Takahashi, C. Wen and K. Yamada, *Solid State Ionics*, **1**, 279 (2000).
26. M. Choi, J. Lee and W. Lee, *J. Mater. Chem. A*, **6**, 11811 (2018).
27. J. Y. Koo, S. Hwang, M. Ahn, M. Choi, D. Byun, W. Lee and K. Lu, *J. Am. Ceram. Soc.*, **9**, 3146 (2016).
28. L. Fan, Y. Wang, Z. Jia, Y. Xiong and M. E. Brito, *Ceram. Int.*, **41**, 6583 (2015).
29. Y. K. Du, P. Yang, Z. G. Mou, N. P. Hua and L. Jiang, *J. Appl. Polym.*, **99**, 23 (2006).
30. A. Bigi, A. Ripamonti, G. Cojazzi, G. Pizzuto, N. Roveri and M. Koch, *Int. J. Biol. Macromol.*, **13**, 110 (1991).
31. W. T. Hong, M. Risch, K. A. Stoerzinger, A. Grimaud, J. Suntivich and Y. Shao-Horn, *Energy Environ. Sci.*, **8**, 1404 (2015).
32. H. Lv, Y. Wu, B. Huang, B. Zhao and K. Hu, *Solid State Ionics*, **177**, 901 (2006).

33. W. Lee, H. J. Jung, M. H. Lee, Y.-B. Kim, J. S. Park, R. Sinclair and F. B. Prinz, *Adv. Funct. Mater.*, **22**, 965 (2012).
34. J. Bae, Y. Lim, J.-S. Park, D. Lee, S. Hong, J. An and Y.-B. Kim, *J. Electrochem. Soc.*, **163**, F919 (2016).
35. Y. B. Kim, J. S. Park, T. M. Gür and F. B. Prinz, *J. Power Sources*, **196**, 10550 (2011).
36. J. S. Park, J. An, M. H. Lee, F. B. Prinz and W. Lee, *J. Power Sources*, **295**, 74 (2015).
37. A. Berenov, A. Atkinson, J. Kilner, M. Ananyev, V. Eremin, N. Porotnikova, A. Farlenkov, E. Kurumchin, H. J. M. Bouwmeester, E. Bucher and W. Sitte, *Solid State Ionics*, **268**, 102 (2014).
38. X. Xu, Y. Chen, W. Zhou, Z. Zhu, C. Su, M. Liu and Z. Shao, *Adv. Mater.*, **28**, 6442 (2016).
39. R. Liu, F. Liang, W. Zhou, Y. Yang and Z. Zhu, *Nano Energy*, **12**, 115 (2015).
40. J. I. Jung, H. Y. Jeong, M. G. Kim, G. Nam, J. Park and J. Cho, *Adv. Mater.*, **27**, 266 (2015).
41. Y. Zhu, W. Zhou, Y. Chen, J. Yu, M. Liu and Z. Shao, *Adv. Mater.*, **27**, 7150 (2015).
42. S. A. Lee, S. Oh, J.-Y. Hwang, M. Choi, C. Youn, J. W. Kim, S. H. Chang, S. Woo, J.-S. Bae, S. Park, Y.-M. Kim, S. Lee, T. Choi, S. W. Kim and W. S. Choi, *Energy Environ. Sci.*, **10**, 924 (2017).
43. W. Xu, F. Lyu, Y. Bai, A. Gao, J. Feng, Z. Cai and Y. Yin, *Nano Energy*, **43**, 110 (2018).
44. K. K. Banger, Y. Yamashita, K. Mori, R. L. Peterson, T. Leedham, J. Rickard and H. Sirringhaus, *Nat. Mater.*, **10**, 45 (2011).
45. M. Choi, I. A. M. Ibrahim, K. Kim, J. Y. Koo, S. J. Kim, J.-W. Son, J. W. Han and W. Lee, *ACS Appl. Mater. Interfaces*, **12**, 21494 (2020).
46. S. J. Kim, M. Choi, J. Lee and W. Lee, *J. Eur. Ceram. Soc.*, **40**, 3089 (2020).
47. S. B. Adler, *Chem. Rev.*, **10**, 4791 (2004).
48. F. Baumann, J. Fleig, H. Habermeier and J. Maier, *Solid State Ionics*, **177**, 1071 (2006).
49. Y. Chen, Y. Bu, Y. Zhang, R. Yan, D. Ding, B. Zhao, S. Yoo, D. Dang, R. Hu, C. Yang and M. Liu, *Adv. Energy Mater.*, **7**, 160890 (2017).
50. M. Choi, S. Hwang, S. J. Kim, J. Lee, D. Byun and W. Lee, *ACS Appl. Energy Mater.*, **2**, 4059 (2019).
51. S. W. Baek, J. Bae and Y. S. Yoo, *J. Power Sources*, **193**, 431 (2009).
52. J. G. Lee, M. G. Park, J. H. Park and Y. G. Shul, *Ceram. Int.*, **40**, 8053 (2014).
53. M. Muranaka, K. Sasaki, A. Suzuki and T. Terai, *J. Electrochem. Soc.*, **156**, B743 (2009).
54. Y. L. Yang, A. J. Jacobson, C. L. Chen, G. P. Luo, K. D. Ross and C. W. Chu, *Appl. Phys. Lett.*, **79**, 776 (2001).

Supporting Information

Porous an hollow nanofibers for solid oxide fuel cell electrodes

Minwoo Ahn, Sangyeon Hwang, Seungwoo Han, Mingi Choi, Doyoung Byun†, and Wonyoung Lee†

Department of Mechanical Engineering, Sungkyunkwan University, Suwon 16419, Korea
(*Received 21 March 2020 • Revised 21 May 2020 • Accepted 8 June 2020*)

Table S1. Contributions of the resistances associated with the three frequencies to the total resistance measured at 650 °C

Polarization resistance (Ωcm^2) (Fraction (%))	LF	MF	HF	Total R_p
pNFs	0.00568 (9.86%)	0.04386 (76.12%)	0.00808 (14.02%)	0.05762
gNFs	0.00302 (12.07%)	0.0157 (62.78%)	0.00629 (25.15%)	0.02501

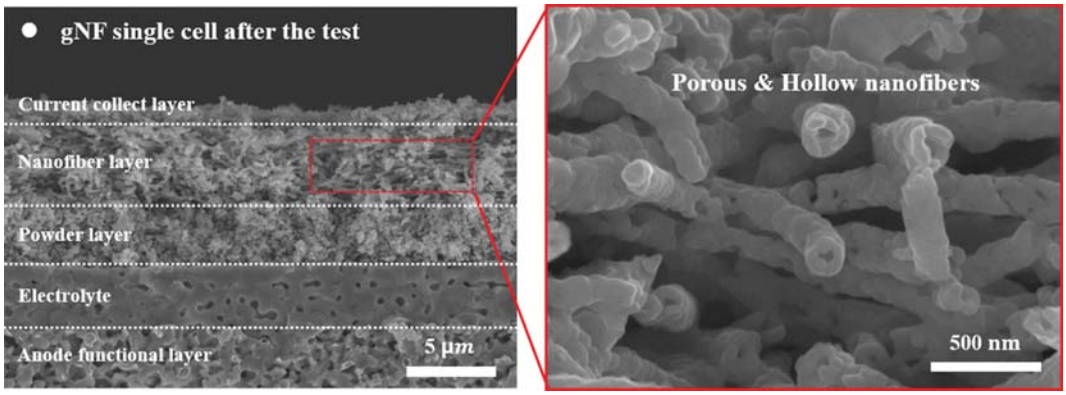

Fig. S1. Cross-sectional SEM images for the gelatin nanofiber-based full cell.

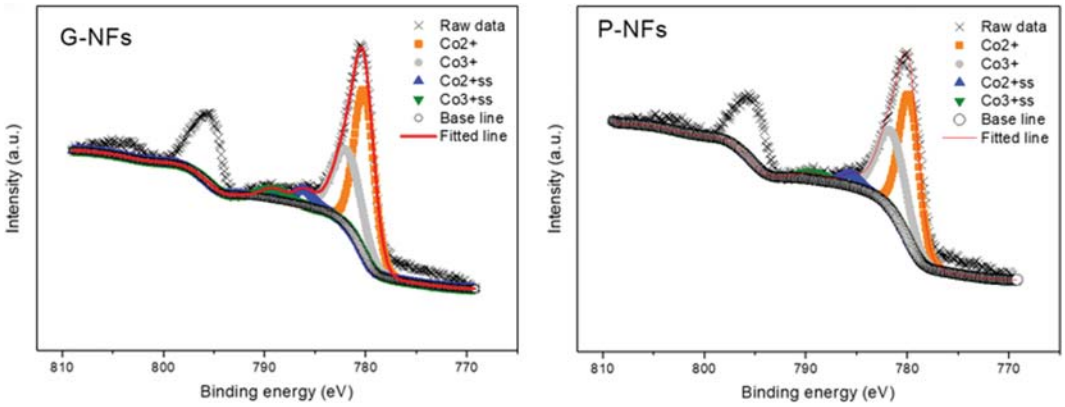

Fig. S2. XPS fitting of Co 2p peak for pNFs and gNFs.

We fitted the Co 2p peak to investigate the reduction state of Co, as shown in Fig. S2. Following the Eq. (1), since more reduced Co is attributed to the formation of oxygen vacancies, higher ratio of Co^{2+}/Co^{3+} value of ~1.52 in gNFs than that in pNFs (~1.29) further supports the higher intensity of oxygen vacancies in gNFs.

$$\text{Reduction of Cobalt } (Co^{3+} \rightarrow Co^{2+}) \qquad 2Co_{Co}^{\times} + O_O^{\times} \rightarrow 2Co_{Co}^{\prime} + V_O^{\cdot\cdot} \qquad (1)$$